RSC Advances

PAPER

View Article Online
View Journal | View Issue

Check for updates

Cite this: *RSC Adv.*, 2025, **15**, 43891

Electroporation in lipid vesicles by varying PEG-grafted lipids in their membranes: an experimental and simulation study

Malay Kumar Sarkar,[ab] Md. Atikur Rahman,[a] Tawfika Nasrin[a] and Mohammad Abu Sayem Karal *[a]

Polyethylene glycol (PEG)-grafted phospholipids alter the mechanical stability of membranes, which may greatly influence the electroporation behavior of PEG-grafted membranes. However, the underlying mechanism of electroporation in a lipid bilayer containing varying mole% of PEG-lipids remains unclear. In this study, we present both experimental observations and molecular dynamics (MD) simulations to investigate the electroporation process and its associated biophysical properties. Initially, the rupture behavior of giant unilamellar vesicles (GUVs) incorporating different mol% of PEG-grafted phospholipids was examined under a constant membrane tension of 5 mN m^{-1}. Results showed that with the increasing PEG-lipid%, the probability and rate constant of rupture increased, while the average survival time of the vesicles decreased, indicating reduced membrane stability. Subsequently, MD simulations were performed to model electroporation in a bilayer with varying PEG-lipid% under a constant DC electric field of 0.4 V nm^{-1}. The time required for electroporation decreased as the PEG-lipid concentration increased. Several physical properties, such as potential energy, solvent accessible surface area (SASA), number of hydrogen bonds (H-bonds), dipole moment, and epsilon and Kirkwood factor, were evaluated. Electroporation was marked by a sharp drop in the potential energy and simultaneous increase in SASA, H-bonds, dipole moment, and dielectric constant, collectively capturing the destabilization and pore formation process at the molecular level. The simulation results were in full agreement with the experimental findings. Alterations in membrane fluidity, electrostatic characteristics, and mechanical stability caused by PEG-lipids in the bilayer are the main reasons for the change in the electroporation dynamics. These insights advance our understanding of membrane behavior and contribute to the development of an efficient electroporation technique with significant biotechnological and medical applications.

Received 31st May 2025
Accepted 29th October 2025

DOI: 10.1039/d5ra03862f

rsc.li/rsc-advances

Open Access Article. Published on 11 November 2025. Downloaded on 1/20/2026 5:34:56 PM.
This article is licensed under a Creative Commons Attribution-NonCommercial 3.0 Unported Licence.

1 Introduction

Giant unilamellar vesicles (GUVs) are model cell-sized spherical structures with a single lipid bilayer. GUVs have wide applications in biomedical and biochemical arenas. Polyethylene glycol (PEG) is an inert, hydrophilic, nonionic, flexible polymer chain. PEG-grafted phospholipids have been widely used in cell-like vesicles that are designed as drug release, gene transfer, and DNA/RNA delivery systems for various diseases, ranging from cancer treatment to pain management.[1–3] The grafted PEG increases the stability and decreases the adsorption of liposomes by serum proteins and the immune system, thereby prolonging the circulation lifetime in the blood vessel.[4–6] In contrast, several studies have reported that the incorporation of PEG-grafted phospholipids changes the characteristics of liposome membranes. The presence of PEG-lipids alters the fluidity, ordering and lamellarity of lipid bilayers.[7–9] Mechanical properties such as the bending modulus increases, but the area compressibility modulus and lysis tension values decrease with the increase in chain length and concentration of PEG lipids.[10–12] Physicochemical properties like the permeability of PEGylated liposome membranes decreases with increasing chain length and concentration of PEG-lipids.[13,14]

Electroporation is a technique for creating pores in cell/vesicle membranes using a series of high-voltage micro-to-millisecond electric pulses. Irreversible electroporation (IRE) refers to electroporation that causes permanent membrane damage, leading to cell death and tissue ablation and preventing the resealing of transient pores.[15,16] The IRE technique has been extensively studied due to its non-thermal and minimally invasive nature in cell destruction or tissue ablation.[17–19] It has potential applications in cancer therapy, tumor ablation, gene

[a]*Department of Physics, Bangladesh University of Engineering and Technology, Dhaka 1000, Bangladesh. E-mail: asayem221@phy.buet.ac.bd; Fax: +880-2-58613046; Tel: +880-2-9665613*

[b]*Department of Arts and Sciences, Ahsanullah University of Science and Technology, Dhaka 1208, Bangladesh*

© 2025 The Author(s). Published by the Royal Society of Chemistry

Open Access Article. Published on 11 November 2025. Downloaded on 1/20/2026 5:34:56 PM. This article is licensed under a Creative Commons Attribution-NonCommercial 3.0 Unported Licence.

transfer, and drug delivery.[20–26] However, understanding the factors that influence the dynamics of pore formation induced by an electric field is crucial for optimizing its efficient applications.

Molecular dynamics (MD) simulations are powerful tools for investigating the nanoscale mechanisms of electroporation in lipid membranes at an atomistic level.[27,28] Electric field-induced hydrophilic pore formation in the POPC lipid bilayer has been investigated using MD simulations.[29] Electroporation in cholesterol containing POPC and DOPC lipid membranes has been investigated by MD simulation, and it has been reported that the threshold electric field required to form pores in the membranes increases with increasing cholesterol content in the membranes, but the electroporation kinetics decrease.[30,31] Using MD simulations, the effects of phospholipids and cholesterol on the electroporation of lipid membranes have been examined.[32] MD simulations and the finite element method have been used to investigate the electric field-induced transmembrane voltage in MCF-7 cancer cells.[33]

Phospholipid-based vesicles, particularly GUVs, are used as ideal model systems for studying electroporation processes due to their simple structure, high reproducibility, and ease of observation under optical microscopy. The bilayer structure of GUVs makes them a valuable tool for exploring membrane pore dynamics during IRE.[34–37] The effects of electrostatic interactions, changes in the salt concentration in the buffer, changes in the mole fraction of negatively charged lipids in the membranes, and cholesterol concentration in the membranes on the IRE of GUVs have been investigated.[38,39] In our previous studies, the impact of osmotic pressure across the membrane and sugar concentration in the buffer of the GUV suspension on IRE was revealed.[40,41] The IRE at different negative membrane potentials was investigated.[42]

In our recent study, we investigated nanoparticle-induced mechanical deformation and poration in neutral GUV membranes (*e.g.*, DOPC/PEG-DOPE) and showed that both the fraction of deformed vesicles and poration increased with increasing PEG-grafted lipid content.[43] However, electric field-induced pore formation in PEG-grafted GUVs, which involves a fundamentally different mechanism in GUV membranes, has not yet been investigated. Recent efforts have demonstrated that locally induced laser-triggered shockwaves can selectively perforate cargo-loaded PEG-grafted GUVs, enabling controlled release without full vesicle rupture.[44] Although this approach highlights the potential of mechanical perturbations for precision membrane disruption, it does not directly address how the presence of PEG-grafted lipids influences rupture dynamics under electrical stress. It has also been reported that increasing PEG-lipid content leads to higher membrane viscosity of PEG-anchored lipids to the DPPC/DOPC/CHOL ternary GUVs, especially in the brush regime, where polymer chains overlap, suggesting reduced lateral mobility and increased mechanical resistance.[45] Although this study provided valuable insights into how grafted polymers modulate membrane dynamics under passive conditions, it did not examine how such changes affect membrane behavior under active stress, such as electroporation. Moreover, the influence of PEG-grafted lipid concentration on the electroporation of charged lipid membranes (*e.g.*, DOPG/DOPC/PEG-DOPE), which are more relevant to biological systems, remains underexplored.

Since the incorporation of PEG-lipids modifies the mechanical and physicochemical properties of liposome membranes, it is hypothesized that varying concentrations of PEG-grafted phospholipids may affect both the threshold electric field required for IRE and the dynamics of pore formation in the bilayer membrane, ultimately influencing the efficiency of membrane damage.

Although experimental studies provide observable data, MD simulations offer atomic-level insights that are often inaccessible through experiments alone. When combined, these approaches yield a more comprehensive and mechanistic understanding of this phenomenon. In this study, we focused on the electroporation behavior of charged DOPG/DOPC/PEG-DOPE-GUVs by integrating experimental and MD simulation approaches to understand how the PEG-lipid content modulates poration kinetics and membrane stability under constant electric tension. This combination creates a powerful synergy that enhances our understanding of electroporation systems.

2 Materials and methods

This study was conducted using both experimental approaches and MD simulations. The experimental and simulation methods are briefly described in the following sections.

2.1 Experimental method

2.1.1 Chemicals and reagents. 1,2-Dioleoyl-*sn-glycero*-3-phospho-(1′-*rac*-glycerol) (sodium salt) (DOPG), 1,2-dioleoyl-*sn-glycero*-3-phosphocholine (DOPC) and 1,2-dioleoyl-*sn-glycero*-3-phosphoethanolamine-*N*-[poly-(ethylene glycol)-2000] (PEG-DOPE) lipids were purchased from Avanti Polar Lipids Inc. (Alabaster, AL). 1,4-Piperazinediethanesulfonic acid (PIPES), ethylene glycol-bis(2-aminoethylether)-*N*,*N*,*N*′,*N*′-tetraacetic acid (EGTA), calcein (bis[*N*,*N*-bis(carboxymethyl)aminomethyl] fluorescein), bovine serum albumin (BSA), sodium chloride (NaCl), sodium hydroxide (NaOH), glucose ($C_6H_{12}O_6 \cdot H_2O$), and sucrose ($C_{12}H_{22}O_{11}$) were purchased from Sigma-Aldrich (Germany).

2.1.2 Preparation of GUVs. GUVs were prepared using a widely used natural swelling method.[46,47] In this method, a total volume of 200 μL mixture of 1 mM DOPC, DOPG and PEG-DOPE lipids dissolved in chloroform was placed into a glass vial of 4.5 mL. The molar ratios of DOPG, DOPC and PEG-DOPE lipids were 20 : 80 : 0, 20 : 77 : 3, and 20 : 75 : 5, respectively. Each lipid combination was dried separately by a mild flow of nitrogen gas, resulting in the formation of lipid films at the bottom of the glass vial. The lipid films were then vacuumed overnight in a desiccator connected to a rotary vacuum pump. An amount of 20 μL Milli-Q water was added into the vial and pre-hydrated for 8 minutes at 45 °C. After pre-hydration, 1 mL calcein (fluorescent dye) solution of 1 mM containing 100 mM sucrose in buffer (10 mM PIPES, 150 mM NaCl, pH 7.0, 1 mM EGTA) was incorporated with the sample

© 2025 The Author(s). Published by the Royal Society of Chemistry

Open Access Article. Published on 11 November 2025. Downloaded on 1/20/2026 5:34:56 PM.
This article is licensed under a Creative Commons Attribution-NonCommercial 3.0 Unported Licence.

and incubated for 2.5 hours at 37 °C to produce a GUV suspension.

The lipid aggregates along with multilamellar vesicles were then subtracted by centrifuging the suspension of GUVs at 13 000 × g, where g is the gravitational acceleration, at 20 °C for 20 minutes by means of a refrigerated centrifuge (NF 800R, NUVE, Turkey). To obtain similar-sized GUVs, the supernatant was filtered through a 10 μm diameter pore nucleopore polycarbonate membrane (Whatman® Nuclepore™ Track-Etched Membranes, UK) clamped in a polypropylene filter holder (Swinnex, ϕ = 25 mm, Millipore Co., Billerica, MA) using the membrane filtering method[48] in a buffer containing 100 mM glucose. An illustration of the DOPG/DOPC/PEG-DOPE-GUV membrane along with the chemical structure of the PEG-DOPE lipid molecule is depicted in Fig. 1.

2.1.3 Irreversible electroporation (IRE) of GUVs. The process of pore formation in the GUV membrane by an electric field is briefly discussed before the method of IRE of GUVs. When an external electric field E is applied to a 'single GUV' of radius R, the internal and external free charges in the buffer are polarized across the membrane because of its impermeable nature to ions. The time required to accumulate free charges is obtained using the Maxwell–Wagner equation.[36,37] The accumulation of charges generates a transmembrane potential, V_m, which induces lateral tension, σ_c, in the GUV membrane. The lateral tension defined by the Maxwell stress tensor is obtained using the following equation:[49–51]

$$\sigma_c = \varepsilon_m \varepsilon_0 \left(\frac{h}{2h_e^2}\right) V_m^2, \quad (1)$$

where the maximum value of $V_m = 1.5RE$ by considering the membrane charging time $\tau_{charg} \approx 0$,[49,52] ε_m (∼4.5) is the membrane's permittivity,[52–54] ε_0 is the free space permittivity, h (∼4 nm) is the thickness of the membrane,[55] and h_e (∼2.8 nm) is the membrane dielectric thickness.[55,56] The maximum value of V_m is called the critical membrane voltage, V_c, for the rupture of the GUV. After simplification of eqn (1), the induced lateral tension is as follows:[57]

$$\sigma_c = 22.86R^2E^2 \text{ [mN m}^{-1}\text{]}, \quad (2)$$

where R is in [m] and E is in [V m^{-1}]. Therefore, the critical membrane tension for GUV rupture depends on the applied electric field E and radius R of the GUV.

To perform the IRE of the GUVs, an amount of 300 μL purified GUV suspension was taken into a U-shaped silicon microchamber placed on a slide glass in which two gold-coated electrodes were placed. The microchamber was coated using 0.10% (w/v) BSA dissolved in buffer containing 100 mM glucose to prevent strong attraction between the GUVs and the glass surface. The GUV suspension containing the microchamber was placed under a fluorescence microscope (Olympus IX-73, Japan) with a 20× objective at 25 ± 1 °C to observe the GUVs. To obtain reproducible results, the vesicle suspension was placed into several microchambers. Each microchamber contained many GUVs of different sizes. A 'single GUV' in between the two electrodes was targeted from each microchamber to apply the electric field. The experimental setup for applying an electric field to the GUV is illustrated in Fig. 2.

The magnitude of electric field E required to induce the desired membrane tension for irreversible pore formation was calculated using eqn (2) by measuring the exact size of each targeted 'single GUV'. For example, to induce σ_c = 5 mN m^{-1} across the GUV of R = 14 μm, the magnitude of the electric field E = 334 V cm^{-1}, where V_m = 0.83 V. In the electroporation technique, we followed the 'single GUV' method.[58,59] In this approach, a single GUV was first focused in a microchamber, and its diameter was precisely measured using a measurement software. Then, an appropriate electric field was applied such that the membrane tension of the GUV remained constant (*e.g.*, 5 mN m^{-1}). It should be noted that only one GUV was measured in each microchamber. In one independent experiment, we examined 14–20 GUVs from 14–20 different microchambers.

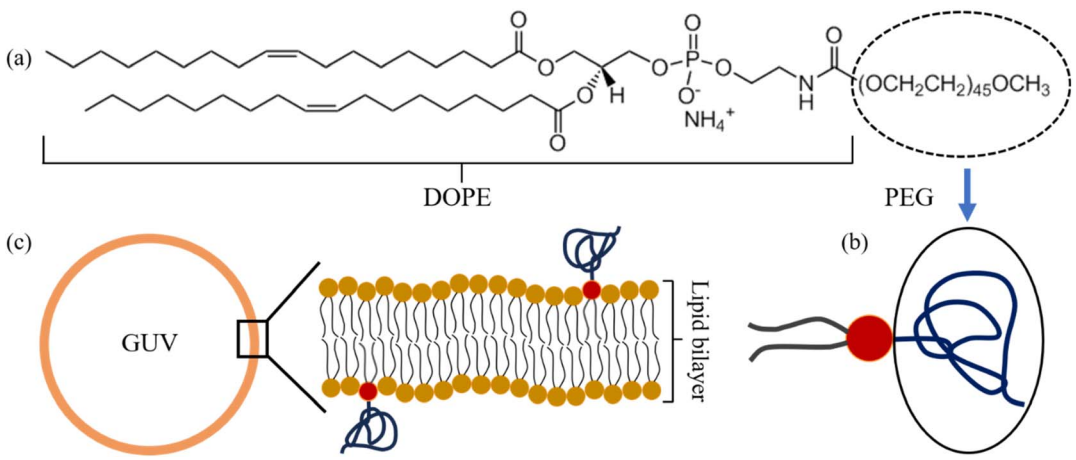

Fig. 1 Structure of PEG-DOPE lipid and schematic of DOPG/DOPC/PEG-DOPE-GUV. (a) Chemical structure of PEG-DOPE lipid with the highlight of the PEG polymer. (b) Illustration of the PEG-DOPE molecule. (c) Schematic of a DOPG/DOPC/PEG-DOPE-GUV with a magnified lipid membrane segment, in which the model arrangement of the PEG-DOPE lipid (red headgroups linked to the arbitrarily twisted long chain of the PEG polymer) is represented.

Open Access Article. Published on 11 November 2025. Downloaded on 1/20/2026 5:34:56 PM.
This article is licensed under a Creative Commons Attribution-NonCommercial 3.0 Unported Licence.

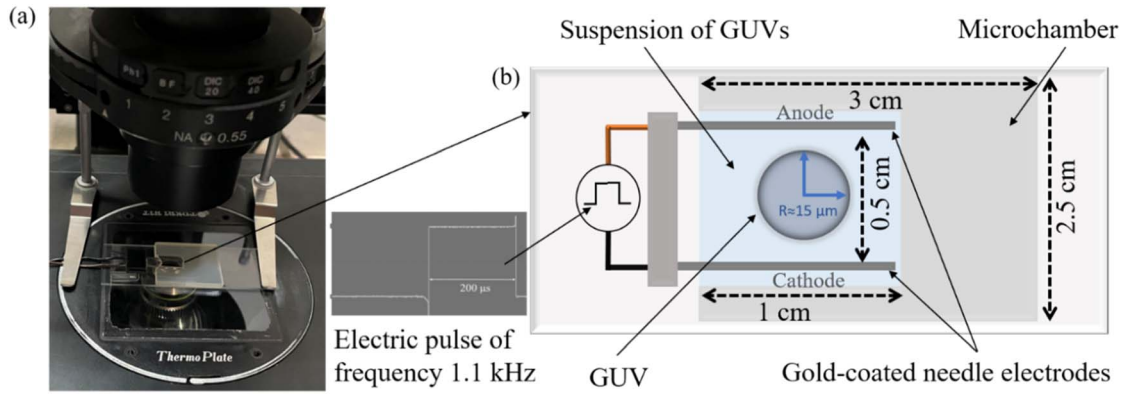

Fig. 2 Experimental setup for the IRE of GUVs. (a) Laboratory set up to observe the IRE of GUVs using an inverted fluorescence microscope. (b) Illustration of applying the electric field to a targeted 'single GUV' in the suspension taken in a U-shaped microchamber placed on a slide glass.

The percentage error in diameter measurement was approximately 2%, which resulted in only about 5% error in the calculated electric field.

The calculated E was applied to the targeted GUV using a series of direct current (DC) pulses of frequency 1.1 kHz and pulse width 200 μs generated by a MOSFET-based circuit in which the electric signal was controlled with a microcontroller. A detailed experimental technique was described in our previous studies.[60] In these experiments, the range of E was 220–360 V cm^{-1} depending on the size of the GUVs. In this experimental procedure, the initial E was set at around 0 V cm^{-1}. Then, the value of E increased rapidly (~7 s) to a desired level and remained constant for 60 s. The rupture of the GUVs due to the applied electric field was observed using a fluorescence microscope and recorded using a charge-coupled device camera (Olympus DP22, Japan) connected with the microscope. The recording speed of the camera was 25 fps. The induced electric tension σ_c across the GUV membrane was constant because a specific value of electric field E was applied for a particular value of radius R.

2.2 Molecular dynamics (MD) simulation method

For the MD simulations, the GROMACS 2024.2 version and PyMOL[61,62] software packages were used. To investigate the effects of PEG-grafted lipid content on the mechanism of pore formation in a lipid bilayer induced by the constant DC electric field, DOPG/DOPC/PEG-DLGL (20/80/0), DOPG/DOPC/PEG-DLGL (20/77/3), and DOPG/DOPC/PEG-DLGL (20/75/5) lipid bilayers along with interfacial water were designed using the CHARMM-GUI input generator.[63,64] Charmm36m all-atom force field[65] was used to compute the molecular interactions. The water/membrane/water model containing TIP3 water molecules has significant stability and is very suitable for observing electroporation, particularly the dielectric constant and dipole moment. The bilayer was designed with a total of 400 DOPG, DOPC and PEG-DLGL lipid molecules in both the upper and lower leaflets of the bilayer, maintaining molar ratios of 20 : 80 : 0, 20 : 77 : 3 and 20 : 75 : 5. All the lipids are randomly distributed throughout the upper and lower leaflets. To neutralize the system, K^+ and Cl^- ions were also incorporated. In the DOPG/DOPC/PEG-DLGL (20/77/3) bilayer, 80 DOPG, 308 DOPC, and 12 PEG-DLGL lipid molecules were used in the upper and lower leaflets along with 20 645 interfacial water molecules, 136 Na^+ ions, and 56 Cl^- ions, while 80 DOPG, 300 DOPC, and 20 PEG-DLGL lipid molecules in the upper and lower leaflets along with 20 717 interfacial water molecules, 136 Na^+ ions, and 56 Cl^- ions were used in the DOPG/DOPC/PEG-DLGL (20/75/5) bilayer. Only 80 DOPG and 320 DOPC lipid molecules were taken in the upper and lower leaflets along with 18 317 interfacial water molecules, 127 Na^+ ions and 45 Cl^- ions to design the DOPG/DOPC/PEG-DLGL (20/80/0) bilayer. The water/membrane/water system was embedded into a cubic box with a dimension of 11.56 nm × 11.56 nm × 7.87 nm, where the box's dimension was slightly changed depending on the different lipid compositions.

In our experimental approach, PEG-DOPE was used as the PEGylated lipid, while PEG-DLGL was employed in the simulations. This choice was primarily guided by the computational feasibility and availability of reliable force-field parameters for PEG-DLGL, which has been well-validated in MD studies. PEG-DOPE and PEG-DLGL share similar structural features; both consist of a hydrophobic lipid tail and a PEG chain, and the exact chemical nature of the lipid headgroup differs, which could influence membrane packing, curvature, and local dynamics.

Particle Mesh Ewald using Fast Fourier Transform (PME FFT) was automatically chosen to generate grid information that balanced the electrostatic potential. Long-range electrostatics were computed using the PME11 algorithm with FFT. Reciprocal-space interactions were evaluated on a 0.168 nm grid using fourth-order B-spline interpolation.[66] A three-dimensional boundary condition was applied in the system. The LINCS10 algorithm constrained hydrogen bond lengths. The NPT ensemble (also known as the isothermal–isobaric ensemble) was used to maintain proper control over pressure and temperature. The initial membrane tension was set to 0 mN m^{-1}, and the temperature was kept constant at 298.15 K. Each system was equilibrated for 10 ns. The energy minimization was carried out using a "steep" algorithm to a maximum allowed force of 1000 kJ mol^{-1} nm^{-1} to prepare the system for

© 2025 The Author(s). Published by the Royal Society of Chemistry

Open Access Article. Published on 11 November 2025. Downloaded on 1/20/2026 5:34:56 PM. This article is licensed under a Creative Commons Attribution-NonCommercial 3.0 Unported Licence.

the production step. Each system was equilibrated with a relaxation time of 1 ps, and a pressure bath at 1 bar, with a relaxation time of 5 ps, utilizing the stochastic V-rescale (a Berendsen thermostat)[67] and C-rescale algorithms.[68] Equilibration of the system was assured by achieving a stable area per lipid. The pressure was coupled semi-isotropically with normal compressibility of 4.5×10^{-5} bar^{-1} in the plane of the membrane.

The production simulations were carried out using the "md" integrator. A time step of 2 fs was employed. Short-range electrostatic and van der Waals interactions were truncated at 1.2 nm. The parameter Ewald_rtol, which governs the relative error for the Ewald sum in both direct and reciprocal spaces, was set to 10^{-5}.

A side view of the designed lipid bilayer is shown in Fig. 3a. A constant DC electric field of 0.4 V nm^{-1} was applied normal (along the z-axis) to the membrane to impose the electrical force on the membrane (Fig. 3b) at a temperature of 298.15 K. In the MD simulation, the time evolution of atomic positions and velocities was governed by Newton's equations of motion. The forces were calculated according to the following equation: $\vec{F} = -\nabla U + q\vec{E}$, where q is the charge of an atom, U is the interatomic potential, and $\vec{E}$ is the electric field. The potential energy was computed using force field parameters comprised bonded and non-bonded interactions.[33] Non-bonded interactions include Lennard-Jones (van der Waals) and Coulomb potentials, while bonded interactions comprise bond stretching, angle bending and dihedral angles. The equation of the total potential energy is

$$U = \sum_{\text{bond}} k_1 (r - r_{\text{eq}})^2 + \sum_{\text{angles}} k_2 (\phi - \phi_{\text{eq}})^2 + \sum_{\text{dihedrals}} \frac{V_n}{2} (1 + \cos(n\varphi - \gamma)) + \sum_{\text{nonbonded}} \left[4\varepsilon_{ij} \left(\left(\frac{c_{ij}}{r_{ij}} \right)^{12} - \left(\frac{c_{ij}}{r_{ij}} \right)^{6} \right) + \frac{q_i q_j}{\varepsilon r_{ij}} \right], \quad (3)$$

where k_1, k_2, and V_n are force constants; n is dihedral multiplicity; r, ϕ, and φ are structural parameters; r_{eq} and ϕ_{eq} are equilibration structural parameters; and γ is the phase angle for torsional angle parameters. ε_{ij} is the depth of the potential well (usually referred to as "dispersion energy"), ε is the potential constant, c_{ij} is the distance at which the particle–particle potential energy U is zero (often referred to as "size of the particle"), r_{ij} is the distance between two interacting particles, and q_i and q_j are particle charges.

3 Results and analysis

The results from the experimental observations and MD simulations are presented in this section.

3.1 Experimental results

To explore the effect of PEG-grafted phospholipids on the IRE of GUVs, the rupture of DOPG/DOPC/PEG-DOPE-GUVs by varying 0%, 3%, and 5% PEG-DOPE in the membranes was observed at constant electric tension $\sigma_c = 5$ mN m^{-1}. The probability of rupture, average survival time, and the rate constant of rupture of GUVs are also presented.

3.1.1 Rupture of GUVs at constant electric tension. A representative experimental result of vesicle rupture for different PEG-DOPE is presented in Fig. 4. First, a constant tension of value $\sigma_c = 5$ mN m^{-1} was applied to a 'single DOPG/DOPC/PEG-DOPE (20/80/0)-GUV' for a maximum of 60 s. In this case, before applying the tension (*e.g.*, time at 0 s), the contrast of the fluorescence microscopic image of the GUV was high due to the calcein-containing sucrose inside the GUV. In the presence of σ_c, the GUV became intact, with a spherical shape of up to 25 s. At 45.5 s, the GUV began to rupture, and at 46 s, the GUV was completely ruptured; the spherical structure had permanently disappeared (Fig. 4a). The same electric tension was then applied to a 'single DOPG/DOPC/PEG-DOPE (20/77/3)-GUV' and 'single DOPG/DOPC/PEG-DOPE (20/77/5)-GUV' in a similar manner. In the presence of σ_c, the DOPG/DOPC/PEG-DOPE (20/77/3)-GUV started to rupture at 22 s and completely ruptured at 23 s (Fig. 4b). Similarly, DOPG/DOPC/PEG-DOPE (20/75/5)-GUV started to rupture at 8 s, and at 10 s, it was completed (Fig. 4c). In our previous studies, we described the process of GUV rupture, beginning with the creation of a nanopore in the membranes that quickly expanded to infinity, resulting in the complete rupture of GUV.[60,69]

3.1.2 Probability of rupture of GUVs. We investigated several GUVs (the number of examined GUVs, N = 14–20) in each lipid combination (*e.g.*, DOPG/DOPC/PEG-DOPE (20/80/0)) in an independent experiment under the same electric tension.

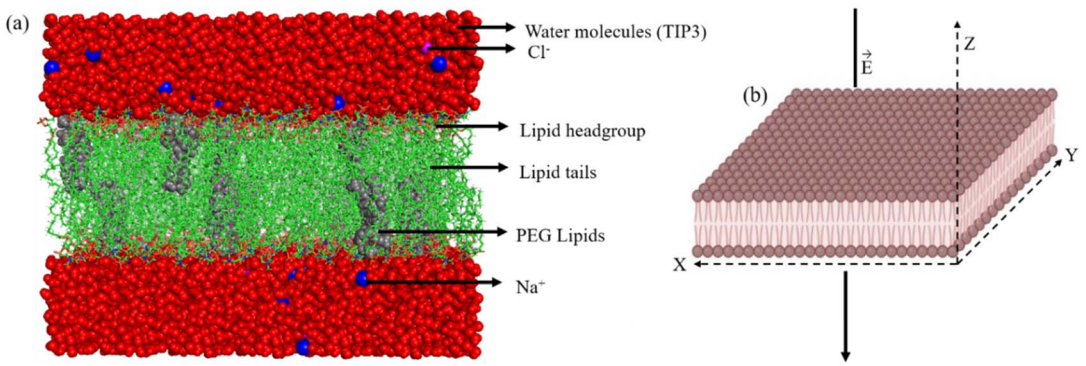

Fig. 3 (a) Side view of a PEGylated lipid bilayer. (b) Direction of the application of a constant DC electric field on a 3D lipid bilayer membrane.

Open Access Article. Published on 11 November 2025. Downloaded on 1/20/2026 5:34:56 PM.
This article is licensed under a Creative Commons Attribution-NonCommercial 3.0 Unported Licence.

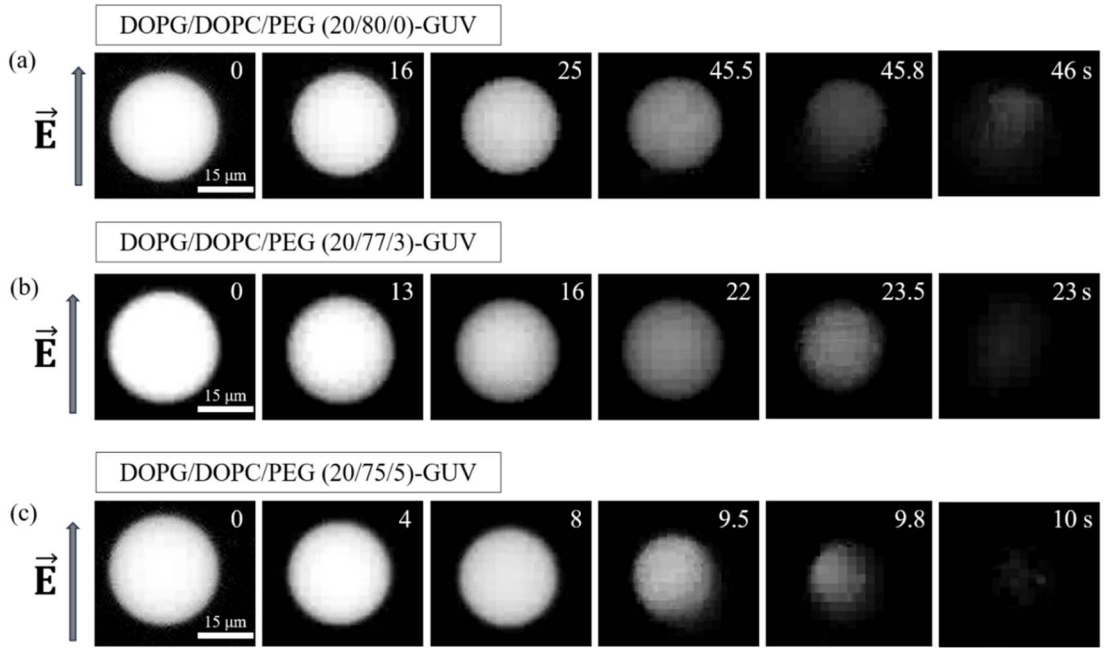

Fig. 4 Fluorescence microscopic image of rupture of a (a) DOPG/DOPC/PEG-DOPE (20/80/0)-GUV (b) DOPG/DOPC/PEG-DOPE (20/77/3)-GUV, and (c) DOPG/DOPC/PEG-DOPE (20/75/5)-GUV under $\sigma_c = 5$ mN m^{-1}. The arrow on the left side indicates the electric field direction. The numbers in each image indicate the time in seconds.

In addition, several independent experiments (the number of independent experiments, n = 3–5) were performed for each case. Here, we present the results obtained from one independent experiment. The time at which the pores begin to form is defined as the time at which the vesicles initiate their rupture. The time of rupture for several GUVs in one independent experiment for each condition is shown in Fig. 5. This shows that 10 out of 14 for DOPG/DOPC/PEG-DOPE (20/80/0)-GUVs, 13 out of 15 for DOPG/DOPC/PEG-DOPE (20/77/3)-GUVs, and all the DOPG/DOPC/PEG-DOPE (20/75/5)-GUVs are ruptured at $\sigma_c = 5$ mN m^{-1}. The rupture of several 'single GUVs' occurred at different times under each condition, *i.e.*, it followed a stochastic nature.

Now, we determined the probability of rupture (P_{rup}) for these membranes. The above results reflect that the concentration of PEG influences the average P_{rup} obtained from 3–5 independent experiments. The average values of P_{rup} with standard deviation were 0.71 ± 0.01, 0.87 ± 0.04, and 1 at $\sigma_c = 5$ mN m^{-1} for 0%, 3%, and 5% PEG-DOPE in the membranes, respectively. Thus, the P_{rup} increases with increasing PEG-grafted lipid concentration, as shown in Fig. 6a. The rupture time of individual GUVs is defined as the survival time (t_{sur}) of the GUVs. The average value of t_{sur} was calculated for each independent experiment. The average values of t_{sur} with standard deviation within 60 s at $\sigma_c = 5$ mN m^{-1} for 0%, 3%, and 5% PEG-DOPE in the membranes were 31.06 ± 2.28, 18.28 ± 2.52 and 11.78 ± 1.10 s, respectively. Therefore, the t_{sur} decreases with the increase in PEG-DOPE (Fig. 6b).

3.1.3 Rate constant of rupture of the GUVs. To calculate the rate constant of rupture (k_p) of the GUVs due to electric tension, the time-dependent fraction of intact GUVs without rupture among all the examined GUVs, P_{intact}, was determined. The P_{intact}, which basically indicates the fraction of intact GUVs after time t, is defined as $P_{intact}(t) = 1 - P_{rup}$.[70,71] The time courses of P_{intact} for DOPG/DOPC/PEG-DOPE (20/80/0)-GUVs, DOPG/DOPC/PEG-DOPE (20/77/3)-GUVs, and DOPG/DOPC/PEG-DOPE (20/75/5)-GUVs at σ_c = 5 mN m^{-1} are shown in Fig. 7a.

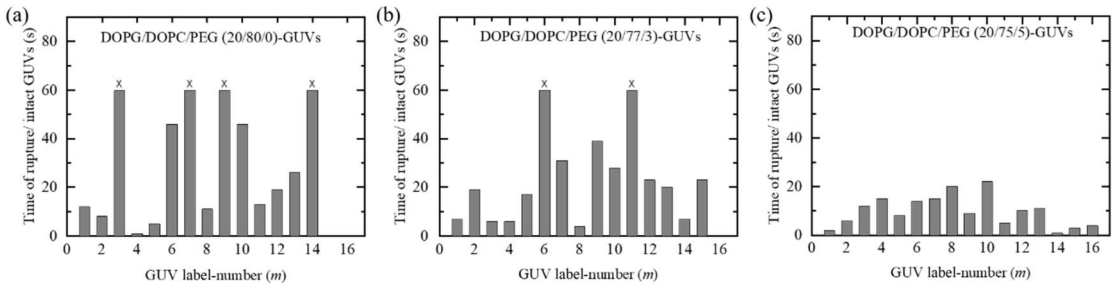

Fig. 5 Stochastic rupture time of several 'single GUVs' at $\sigma_c = 5$ mN m^{-1} containing (a) 0% PEG-DOPE, (b) 3% PEG-DOPE, and (c) 5% PEG-DOPE in their membranes. The (×) mark at the top of the bar indicates that the GUV did not rupture within 60 s.

© 2025 The Author(s). Published by the Royal Society of Chemistry

Open Access Article. Published on 11 November 2025. Downloaded on 1/20/2026 5:34:56 PM.
This article is licensed under a Creative Commons Attribution-NonCommercial 3.0 Unported Licence.

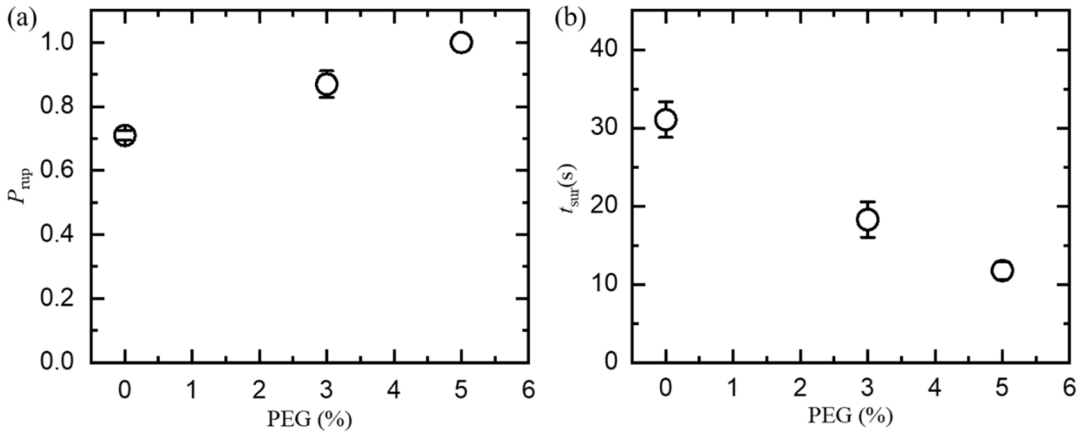

Fig. 6 PEG-DOPE% dependent probability of rupture and average survival time of GUVs at $\sigma_c = 5$ mN m^{-1}. (a) Probability of rupture and (b) average survival time. Error bar represents the standard deviation (SD) obtained from 3–5 independent experiments.

The experimental data were fitted by a single-exponential decay function (solid line depicted in Fig. 7a) defined as follows:

$$P_{\text{intact}}(t) = \exp(-k_p t), \quad (4)$$

where k_p is the rate constant of rupture and t is the duration of the constant electric tension applied to the GUVs. From the fitted curves, the values of k_p were determined to be 0.026, 0.063, and 0.085 s^{-1} for 0%, 3%, and 5% PEG-DOPE in the GUV's membrane, respectively. Similar experiments were performed for several cases ($n = 3$–5), and the average values of k_p were calculated. The average k_p increases with increasing the concentration of PEG-grafted lipid, as illustrated in Fig. 7b.

3.2 Molecular dynamics (MD) simulation results

Electroporation involves rapid nanoscale events, such as pore formation, membrane deformation, water penetration, and lipid rearrangement, all occurring within nanoseconds. MD simulations are essential for studying electroporation, as they provide atomic-level insights into dynamic processes that are difficult or impossible to observe experimentally. This section presents the results of the dynamics of electroporation in the DOPG/DOPC/PEG-DLGL bilayer containing 0%, 3%, and 5% PEG-DLGL using a constant DC electric field of 0.4 V nm^{-1} with MD simulations. It also presents the results of the variation of solvent accessible surface area (SASA) in the bilayer, number of hydrogen bonds (H-bonds) in the interfacial water molecules, potential energy of the water/bilayer/water system, dipole moment of interfacial water, and epsilon and Kirkwood factor during electroporation.

3.2.1 Dynamics of electroporation in the lipid bilayer. The dynamics of electroporation induced by a constant DC electric field of 0.4 V nm^{-1} in the DOPG/DOPC/PEG-DLGL (20/80/0), DOPG/DOPC/PEG-DLGL (20/77/3), and DOPG/DOPC/PEG-DLGL (20/75/5) bilayers are presented in Fig. 8. At 0.00 ns, the bilayers were intact, with no visible pores (Fig. 8a), indicating that the interfacial water molecules were separated by the lipid bilayers at that time (Fig. 8b). A small number of water molecules began to penetrate the DOPG/DOPC/PEG-DLGL (20/80/0) bilayer at 3.33 ns, which connected the upper and lower water

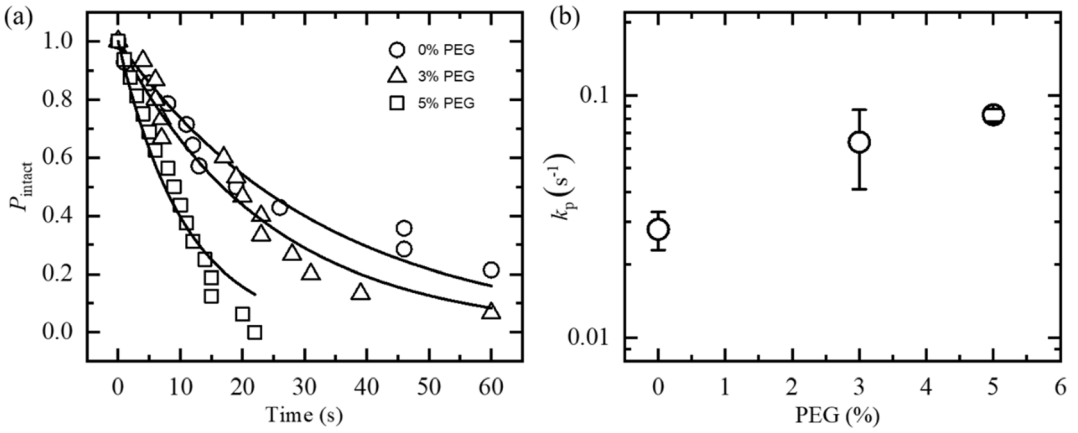

Fig. 7 (a) Time course of the fraction of intact GUVs containing various PEG-DOPE% at $\sigma_c = 5$ mN m^{-1}. The solid lines represent the best-fitted single exponential decay function of eqn (4). The goodness of fit was evaluated using the coefficient of determination (R^2). The R^2 values were 0.95, 0.96, and 0.95 for 0%, 3%, and 5% PEG-DOPE, respectively. (b) PEG-DOPE% dependent rate constant of rupture of GUVs. Error bar represents the standard deviation (SD) obtained from 3–5 independent experiments.

Open Access Article. Published on 11 November 2025. Downloaded on 1/20/2026 5:34:56 PM.
This article is licensed under a Creative Commons Attribution-NonCommercial 3.0 Unported Licence.

layers, marking the initiation of pore formation. The pore size increased over time, reaching a maximum of 3.73 ns, which indicated the formation of a transmembrane pore in the DOPG/DOPC/PEG-DLGL (20/80/0) bilayer. In the DOPG/DOPC/PEG-DLGL (20/77/3) bilayer, pore initiation occurred at 2.40 ns, and a full transmembrane pore was formed by 2.78 ns. In the DOPG/DOPC/PEG-DLGL (20/75/5) bilayer, pore initiation was observed at 2.10 ns, with a transmembrane pore forming at 2.60 ns. The average values with standard deviation of transmembrane pore formation time obtained from 3 independent experiments were 3.70 ± 0.26, 2.33 ± 0.23, and 2.03 ± 0.29 ns for 0, 3, and 5% PEG-DLGL, respectively. These results demonstrate that the time required for pore formation under a constant DC electric field increases with higher

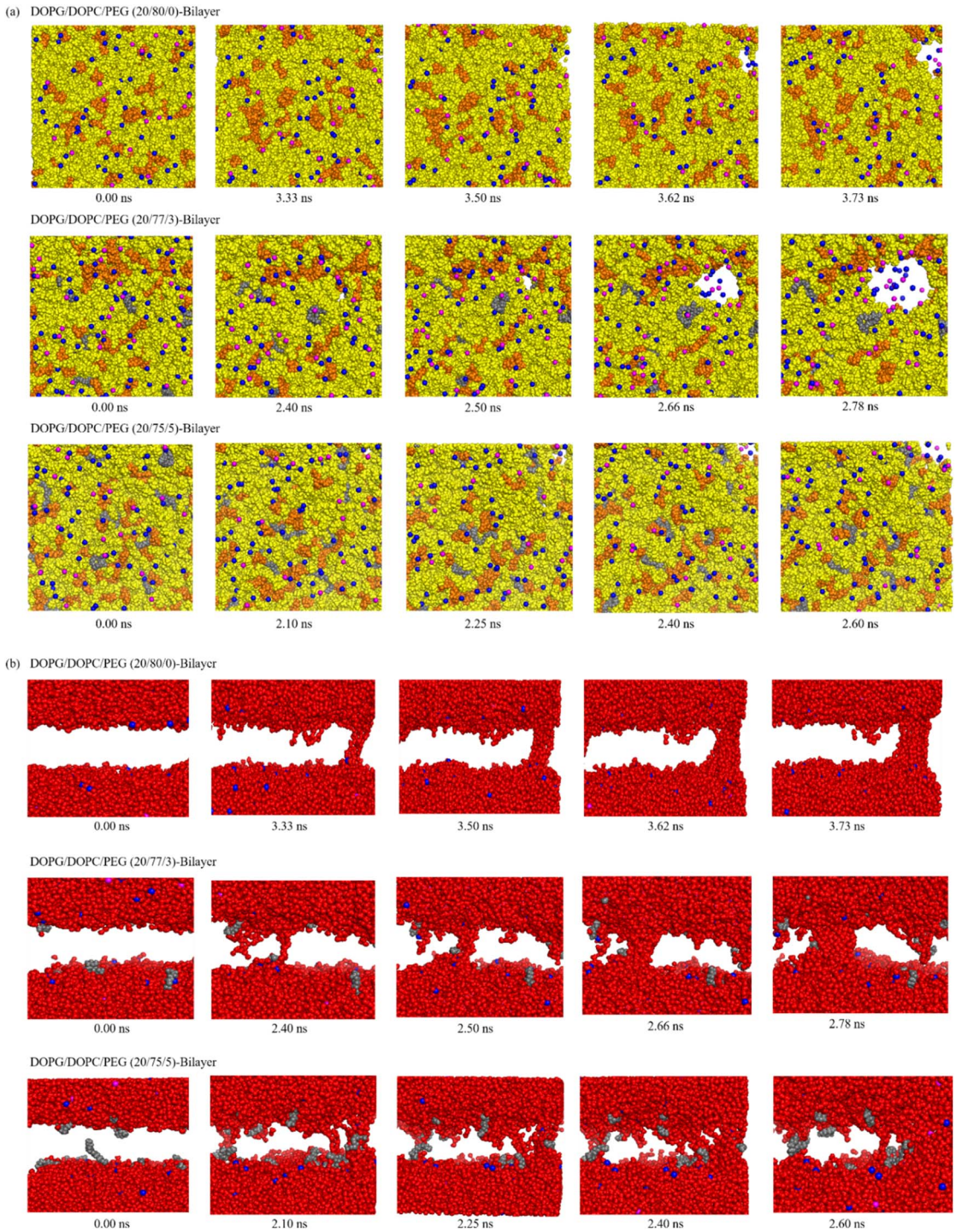

Fig. 8 Dynamics of pore formation by a constant DC electric field of 0.4 V nm^{-1} in the DOPC/DOPG/PEG-DLGL bilayer. (a) Top view of the lipid bilayer, where the yellow, orange, and gray spheres indicate the DOPC, DOPG, and PEG-DLGL lipids, respectively. Blue and magenta spheres indicate the Na^+ and Cl^- ions, respectively. (b) Side view of water molecules inside and outside the lipid bilayer (blank space), which is hidden.

© 2025 The Author(s). Published by the Royal Society of Chemistry

Open Access Article. Published on 11 November 2025. Downloaded on 1/20/2026 5:34:56 PM. This article is licensed under a Creative Commons Attribution-NonCommercial 3.0 Unported Licence.

concentrations of PEG-DLGL in the lipid bilayer, which is fully consistent with the experimental observations.

MD simulations are inherently limited to very short timescales, typically on the order of nanoseconds to microseconds, due to computational constraints. In contrast, experimental processes, such as electroporation or membrane rupture, often occur over much longer timescales, from seconds to minutes. Therefore, the rupture times observed in MD simulations (2–3 ns) are not directly comparable to experimental rupture times (~10–45 s).

3.2.2 Potential energy of the bilayer–water system during electroporation. The potential energy of a bilayer system is a crucial parameter for understanding membrane stability and behavior under external stimuli. It is generally observed that the formation of a porous defect within the bilayer, indicating structural destabilization, is accompanied by a sudden drop in the system's potential energy. Fig. 9 shows the variation in potential energy over time for DOPG/DOPC/PEG-DLGL bilayer–water systems subjected to a constant DC electric field of 0.4 V nm^{-1}. For the DOPG/DOPC/PEG-DLGL (20/80/0) bilayer, the potential energy exhibits a sharp decrease at approximately 3.5 ns, signaling the onset of membrane disruption. In contrast, the systems containing 3% and 5% PEG-DLGL show earlier energy drops at around 3.0 ns and 2.75 ns, respectively. This progressive reduction in the time to energy collapse suggests that increasing the PEG-DLGL content accelerates the development of structural flaws within the bilayer. Consequently, PEG-DLGL appears to facilitate bilayer destabilization under an electric field likely by modifying the membrane's mechanical integrity or promoting pore formation.

3.2.3 Solvent accessible surface area (SASA) in the bilayer during electroporation. SASA, through which the solvent can easily access, displayed a significant response during electroporation in the bilayer, as shown in Fig. 10. In the case of DOPG/DOPC/PEG-DLGL (20/80/0) bilayer, SASA slightly increased up to 3.5 ns from 725 nm^2 to 825 nm^2; then, it rapidly increased to 1000 nm^2 within a very short time of 1.25 ns. After that, the value of SASA decreased slightly, indicating destabilization of the system. For DOPG/DOPC/PEG-DLGL (20/77/3) and DOPG/DOPC/PEG-DLGL (20/75/5) bilayers, the variation in SASA followed similar trends. For DOPG/DOPC/PEG-DLGL (20/77/3), SASA slowly increased up to 2.5 ns; then, it started to rapidly increase and reach a maximum value of 1000 nm^2 at 3.5 ns. After 3.5 ns, SASA suddenly decreased due to system disruption. The SASA increased sharply from 2.0 ns and reached a maximum value of 1035 nm^2 at 3.1 ns. Therefore, the time at which the SASA started to increase sharply was minimum for DOPG/DOPC/PEG-DLGL (20/75/5) bilayer and maximum for DOPG/DOPC/PEG-DLGL (20/80/0).

3.2.4 Number of H-bonds in interfacial water during electroporation. The variations in the number of H-bonds during electroporation in the water/bilayer/water system are presented in Fig. 11. In the presence of a constant DC electric field of 0.4 V nm^{-1}, the time of rapid increase in the number of H-bonds decreased with an increase in the PEG-DLGL content in the bilayer. A notable increase in the number of H-bonds was observed at the onset of pore formation in the bilayer. Notably, these findings align closely with the SASA variations shown in Fig. 10, which also demonstrate increased membrane exposure and porosity in response to PEG-DLGL incorporation.

3.2.5 Dipole moment of interfacial water with bilayer during electroporation. When a pore is formed in the lipid bilayer under the influence of an electric field, a continuous water bridge is established across the membrane, leading to a rapid and significant change in the dipole moment of interfacial water molecules. The variation in dipole moment of interfacial water for DOPG/DOPC/PEG-DLGL bilayer under 0.4 V nm^{-1} is shown in Fig. 12. The dipole moment of interfacial water was rapidly increased after 3.5 ns for the DOPG/DOPC/PEG-DLGL (20/80/0), but for the DOPG/DOPC/PEG-DLGL (20/77/3) and DOPG/DOPC/PEG-DLGL (20/75/5) bilayers, it increased after 3.0 ns and 2.75 ns, respectively. This result also

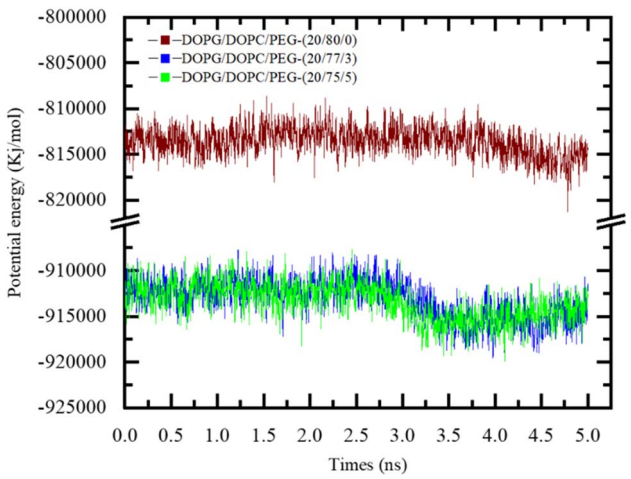

Fig. 9 Variation in the potential energy of the DOPC/DOPG/PEG-DLGL bilayer–water system at a constant DC electric field of 0.4 V nm^{-1}.

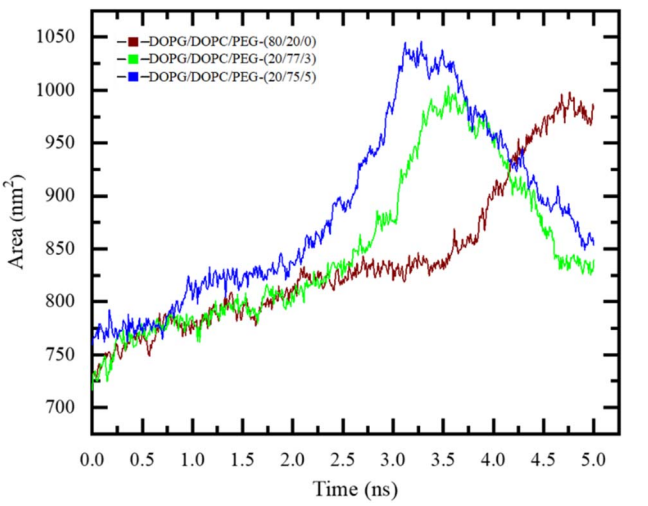

Fig. 10 Variation in SASA with time during electroporation in the DOPC/DOPG/PEG-DLGL bilayer at a constant DC electric field of 0.4 V nm^{-1}.

Open Access Article. Published on 11 November 2025. Downloaded on 1/20/2026 5:34:56 PM. This article is licensed under a Creative Commons Attribution-NonCommercial 3.0 Unported Licence.

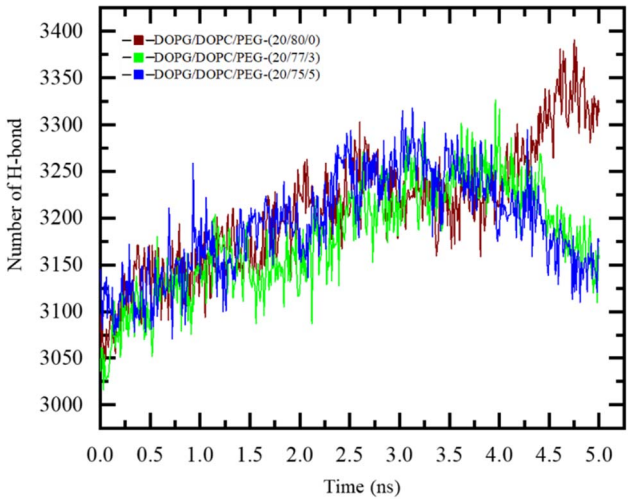

Fig. 11 Variation in the number of H-bonds with time during electroporation in the DOPC/DOPG/PEG-DLGL bilayer at a constant DC electric field of 0.4 V nm^{-1}.

indicates that the PEG-DLGL content in the bilayer reduces the electroporation time at a constant DC electric field.

3.2.6 Epsilon and Kirkwood factor of the bilayer during electroporation. The dielectric constant of interfacial water is a key indicator of its polarization behaviour, and it is closely related to the epsilon and Kirkwood factor, which quantifies the collective orientation correlation of water dipoles. The variation in the epsilon and Kirkwood factor over time for the DOPG/DOPC/PEG-DLGL bilayer under a constant DC electric field of 0.4 V nm^{-1} is presented in Fig. 13. It was observed that the time of rapid increase in the dielectric constant for the DOPG/DOPC/PEG-DLGL (20/75/5) bilayer was the minimum, and it was the maximum for DOPG/DOPC/PEG-DLGL (20/80/0). These changes

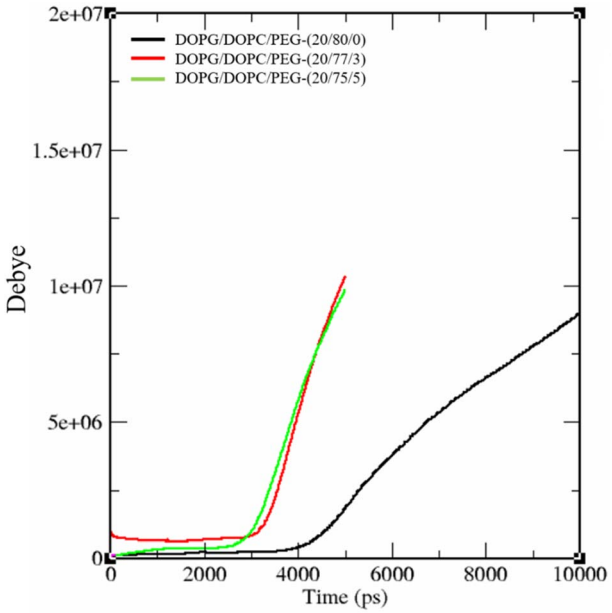

Fig. 12 Variations in the dipole moment of water in the DOPC/DOPG/PEG-DLGL bilayer during electroporation.

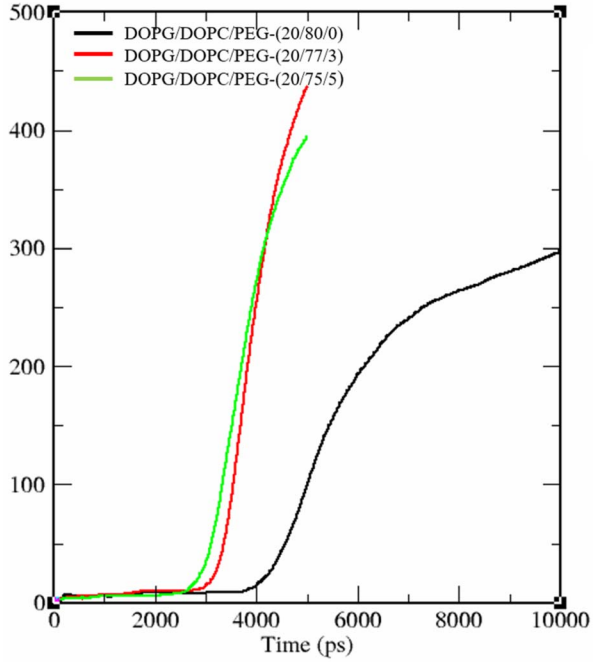

Fig. 13 Variations in the epsilon and Kirkwood factor with time in the DOPC/DOPG/PEG-DLGL bilayer during electroporation.

are well supported by the variation in dipole moment, as shown in Fig. 12. Hence, these results indicate that during electroporation, the formation of a pore and the associated alignment of water molecules in the resulting water bridge significantly influence the epsilon and Kirkwood factor, reflecting enhanced dipolar ordering in the interfacial region.

4 Discussion

First, we investigated the rupture of DOPG/DOPC/PEG-DOPE-GUVs by varying 0–5 mol% PEG-DOPE in the membranes using a constant electric tension (σ_c) of 5 mN m^{-1}. The probability of rupture (P_{rup}), average survival time (t_{sur}), and rate constant of rupture (k_p) were determined by analysing the experimental data. The P_{rup} and k_p increased whereas t_{sur} decreased with the increase in PEG-DOPE in the membranes.

Second, the dynamics of electroporation in the DOPG/DOPC/PEG-DLGL bilayer by varying 0–5 mol% PEG-DLGL at a constant DC electric field of 0.4 V nm^{-1} was also examined using MD simulations. The variation in biophysical parameters such as potential energy, SASA, number of H-bonds, dipole moment, and epsilon and Kirkwood factor during electroporation was evaluated. The poration time decreased with increasing PEG-DLGL% in the bilayer. The biophysical parameters obtained from MD simulations correlate with each other and are well supported by the experimental findings.

It should be mentioned that the surface charge density of a membrane affects the electroporation of GUVs due to electrostatic interactions.[72,73] To keep the surface charge density constant, we used a total of 200 μL mixture of lipids, among which the negatively charged DOPG was 20% in all membranes (already discussed in the GUV preparation section). To isolate

© 2025 The Author(s). Published by the Royal Society of Chemistry

Open Access Article. Published on 11 November 2025. Downloaded on 1/20/2026 5:34:56 PM.
This article is licensed under a Creative Commons Attribution-NonCommercial 3.0 Unported Licence.

the PEG effect, a non-PEG membrane presented as DOPG/DOPC/PEG-DOPE (20/80/0) was investigated.

It is well established that the experimental quantification of transmembrane voltage required for membrane breakdown is around 1.0 V.[36,52] In our study, we obtained a value of around 0.83 V for 5 mN m^{-1}. As the applied electric tension increases, the transmembrane voltage increases. In the MD simulations, we used an optimum field strength of 0.4 V nm^{-1} for all membrane systems, which corresponded to a transmembrane voltage of 1.6 V. Pore formation could also be observed at lower field strengths, *e.g.*, 0.2 V nm^{-1} or 0.3 V nm^{-1}, corresponding to a transmembrane voltage of 0.8 V or 1.2 V; however, it required a longer simulation time. MD simulations are inherently limited to very short timescales, typically on the order of nanoseconds to microseconds, due to computational constraints. Thus, we selected a relatively higher electric field (*e.g.*, 0.4 V nm^{-1}) for the desired output.

It is well established that the rupture probability and rate constant increase with increasing membrane tension, as higher membrane stresses promote the nucleation and expansion of transient pores.[34,42] To systematically investigate the influence of PEG-grafted lipids on this process, we selected an optimum electric tension of 5 mN m^{-1}. This value was chosen because it lies within the range where electroporation occurs with moderate probability, which is high enough to induce measurable pore formation but low enough to avoid immediate membrane rupture. Under such controlled conditions, the subtle effects of varying PEG-lipid content on the frequency and dynamics of pore formation can be clearly distinguished. The chosen tension thus provides a suitable balance between membrane stability and poration sensitivity, enabling a reliable comparison of electroporation behavior across different membrane compositions.

The PEG chain of a phospholipid has a hydrophilic property, and its presence in the bilayer membrane generally increases the hydrophilicity of the lipid bilayer, alters membrane fluidity, and affects the overall structural integrity of the membrane.[7,10,74,75] These modifications can significantly influence the electric field-induced lateral tension across the membranes, which is responsible for the rupture of GUVs. PEG-grafted phospholipids introduce steric repulsion between lipid molecules and reduce the cohesive forces between lipid molecules,[10,76] which makes the membrane more susceptible to mechanical destabilization. When the mole% of PEG-grafted lipid increases, the effect becomes more significant, leading to a greater ease in permeabilizing and rupturing the membrane,[77–79] as shown in Fig. 4. The increase in the P_{rup} with a higher PEG-DOPE lipid is likely due to a decrease in the mechanical strength and increased fluidity of the membrane.[80] The increase in membrane fluidity and decrease in the cohesive forces between lipid molecules lead to a more dynamic and less stable bilayer, which is more prone to pore formation under the electric field (Fig. 6a). As a result, membranes with a higher PEG-DOPE content are more likely to undergo IRE, increasing the rupture kinetics (Fig. 7). Moreover, increased PEGylation can alter the electrostatic properties of the membrane.

PEG's hydrophilic nature reduces the membrane's ability to maintain a high dielectric constant, which is critical in resisting pore formation under electrical stress.[81] The presence of PEG could reduce the energy required to create and maintain pores, resulting in faster and more frequent pore formation, which also accelerates membrane rupture. When the membrane is more fluid and less cohesive, the electroporation process occurs more rapidly.[82] Additionally, PEG chains may lower the energy barrier for pore formation by increasing the membrane's local deformability. This facilitates a quicker response to the applied electric field, leading to faster rupture kinetics.[83,84] Once electroporation occurs, the GUVs are not recovered. This is especially true for vesicles that have a higher PEG concentration, as they exhibit more rapid and extensive pore formation, leading to the leakage of cellular contents and osmotic imbalance, both of which contribute to the reduced survival time,[85,86] as shown in Fig. 6b. Moreover, PEGylation generally enhances membrane permeability, rendering it more vulnerable to osmotic shock after electroporation. The disruption of membrane integrity and the failure to regain the original lipid bilayer configuration after electroporation lead to rupture, consequently shortening the vesicle survival time.

The results of MD simulations show that incorporating PEG-DLGL in the DOPG/DOPC/PEG-DLGL bilayer significantly influences pore formation dynamics. The pore formation time became larger for 0% PEG-DLGL and smaller for 5% PEG-DLGL, as shown in Fig. 8. The variation in time is well explained by the increased hydrophilicity effect of PEG lipids in the bilayer, as discussed in the previous section. During electroporation, the potential energy of the lipid bilayer system typically undergoes a sudden drop, reflecting a major structural change, specifically the formation of a pore in the membrane. Before electroporation, the system remains stable, and the potential energy fluctuates around an equilibrium value as the bilayer resists deformation under the applied electric field.[87] As the electric field stresses the membrane, water begins to penetrate and disrupt the lipid arrangement. When a critical threshold is reached, a hydrophilic pore is formed rapidly.[88,89] This pore formation leads to abrupt structural rearrangements, such as the breaking of lipid–lipid interactions and reorientation of lipids around the pore edge.[90,91] These changes release stored mechanical and electrostatic energy, causing a sharp decrease in potential energy. After the pore is stabilized, the potential energy may plateau again at a lower level, corresponding to a new, less ordered, and more hydrated membrane state.[92,93] The phenomena observed in Fig. 9 are well supported.

SASA changes during electroporation because the structural integrity of the lipid bilayer is disrupted, allowing water molecules to penetrate and interact with regions of the membrane that were previously shielded. As pores begin to form, the internal, normally hydrophobic parts of lipid molecules, including tails and deeper regions of headgroups, become exposed to the aqueous environment.[94–96] This exposure increases the total area of the membrane that is accessible to solvent molecules, resulting in a sharp rise in SASA (Fig. 10). Therefore, a rapid increase in SASA is a clear molecular signature of membrane destabilization and pore formation during

Open Access Article. Published on 11 November 2025. Downloaded on 1/20/2026 5:34:56 PM. This article is licensed under a Creative Commons Attribution-NonCommercial 3.0 Unported Licence.

electroporation.[97] As the membrane becomes destabilized and pores begin to form, the internal regions of the bilayer become increasingly exposed to water. This not only raises the SASA but also allows more water molecules to come into close proximity with lipid headgroups and other water molecules, leading to a surge in H-bond formation (Fig. 11).[98]

The penetration of water into the membrane and the formation of a water bridge across the bilayer also result in the realignment of water dipoles.[99] The net dipole moment of water molecules $\vec{\mu}_{\text{net}} = \sum_{i}^{N} \vec{\mu}_i$, where N is the total number of water molecules in the region of interest and $\vec{\mu}_i$ is the dipole moment of i^{th} water molecule, which is defined as $\vec{\mu}_i = \sum_{j=1}^{3} q_j \vec{r}_{ij}$, where q_j is the partial charge on the atoms of the water molecule and $\vec{r}_{ij}$ is the position vectors of the atoms in the molecule. As more water molecules are involved and their orientations become more aligned in the direction of the electric field, the net dipole moment of the interfacial region increases sharply (Fig. 12) and is similar to the reported data.[32] During pore formation, the number of water molecules near or within the membrane increases, and these water molecules often align more strongly with the electric field or local electrostatic environment. This enhanced alignment leads to an increase in the epsilon and Kirkwood factor, signifying more cooperative dipole orientations among water molecules (Fig. 13).[100] Therefore, the potential energy, SASA, H-bonds, dipole moments, and epsilon and Kirkwood factor were varied during electroporation using MD simulations. Such variations also changed depending on the mole% of PEG lipid content in the bilayer membranes.

These findings have momentous implications for the use of IRE in biotechnological applications, such as gene delivery, drug delivery, and cancer therapy. The increased rate constant of rupture and decreased average survival time in PEGylated GUVs could be utilized to improve the efficiency of drug or gene delivery, particularly when quick and regulated membrane permeabilization is necessary. MD simulations offer a powerful, controlled, and cost-effective platform for understanding the fundamental mechanisms of electroporation and for guiding experimental design and biomedical applications. These findings also suggest that careful optimization of PEG concentration is necessary to balance the desired therapeutic effect with membrane stability.

5 Conclusions

The experimental results of this study reveal that the incorporation of PEG-grafted phospholipids into GUV membranes increases the probability of rupture and the rate constant of rupture and decreases the average survival time of the GUVs at constant electric tension. The results of MD simulations also show that electroporation time decreases with increasing PEG-DOPE% in the bilayer. The potential energy, SASA, H-bonds, dipole moments, and epsilon and Kirkwood factor were varied during electroporation in MD simulations. Such variations also changed depending on the PEG-DLGL% in the bilayer. The experimental and simulation results are fully consistent. These effects are likely due to changes in membrane fluidity, electrostatic properties, and mechanical integrity caused by PEGylation of the GUV membranes. Therefore, this study explores the influence of PEG concentration on electroporation in the PEGylated lipid membrane of GUVs, which may contribute to the development of a more efficient electroporation technique that has important implications in drug delivery, gene transfer, and tissue ablation in medical therapies. Following these findings, further investigation may be performed under different environmental parameters, such as ionic strength, pH, osmotic pressure, and temperature, to assess their synergistic effects with PEG-lipid incorporation on membrane stability. This could provide a more comprehensive understanding of both synthetic systems and biological membranes, which may help in the development of membrane-based technologies in biotechnology and medicine.

Author contributions

M. K. S., M. A. R. and M. A. S. K. designed the work. M. K. S., M. A. R. and M. A. S. K. performed the experiments and analyzed the data. M. K. S., M. A. R. and M. A. S. K. contributed to the theoretical calculation for the experimental design. M. K. S., T. N. and M. A. S. K. wrote the paper, and all authors discussed thoroughly for improving the manuscript.

Conflicts of interest

There is no conflict of interest regarding this work.

Data availability

The data supporting the findings of this study are available upon reasonable request to the corresponding author.

Acknowledgements

This work was supported partly by the Grant for Advanced Research in Education, Ministry of Education, Bangladesh (37.20.0000.004.033.020.2016.1053), special allocation, Ministry of Science and Technology, Bangladesh (39.00.0000.009.99.024.22-901), and Basic Research Grant of Bangladesh University of Engineering and Technology (Est/R-60/Re-5336). The authors acknowledged the CASR-BUET for the approval of research funding (no. 347(25)). The funders had no role in study design, data collection and analysis, decision to publish, or preparation of the manuscript. There was no additional external funding received for this study.

References

1 S. Shahbazi, F. Tafvizi and V. Naseh, *Heliyon*, 2024, **10**, e30503.
2 K. He, T. Wang, J. Chen, X. Huang, Z. Wang, Z. Yang, K. Wang, W. Zhao, J. Jiang and L. Zhao, *Int. J. Nanomed.*, 2023, **18**, 4007–4021.

© 2025 The Author(s). Published by the Royal Society of Chemistry

Open Access Article. Published on 11 November 2025. Downloaded on 1/20/2026 5:34:56 PM. This article is licensed under a Creative Commons Attribution-NonCommercial 3.0 Unported Licence.

3 H. Nsairat, D. Khater, U. Sayed, F. Odeh, A. Al Bawab and W. Alshaer, *Heliyon*, 2022, **8**, e09394.
4 K. Izumi, J. Ji, K. Koiwai and R. Kawano, *ACS Omega*, 2024, **9**, 10958–10966.
5 L. Geng, M. Matsumoto, F. Yao, M. Umino, M. Kamiya, H. Mukai and S. Kawakami, *Eur. J. Pharm. Sci.*, 2024, **203**, 106929.
6 T. M. Allen and P. R. Cullis, *Adv. Drug Deliv. Rev.*, 2013, **65**, 36–48.
7 E. C. Giakoumatos, L. Gascoigne, B. Gumí-Audenis, Á. G. García, R. Tuinier and I. K. Voets, *Soft Matter*, 2022, **18**, 7569–7578.
8 V. Nele, M. N. Holme, U. Kauscher, M. R. Thomas, J. J. Doutch and M. M. Stevens, *Langmuir*, 2019, **35**, 6064–6074.
9 D. Pozzi, V. Colapicchioni, G. Caracciolo, S. Piovesana, A. L. Capriotti, S. Palchetti, S. De Grossi, A. Riccioli, H. Amenitsch and A. Laganà, *Nanoscale*, 2014, **6**, 2782.
10 A. Mahendra, H. P. James and S. Jadhav, *Chem. Phys. Lipids*, 2019, **218**, 47–56.
11 O. Garbuzenko, Y. Barenholz and A. Priev, *Chem. Phys. Lipids*, 2005, **135**, 117–129.
12 D. Marsh, *Biophys. J.*, 2001, **81**, 2154–2162.
13 K. Hashizaki, H. Taguchi, C. Itoh, H. Sakai, M. Abe, Y. Saito and N. Ogawa, *Chem. Pharm. Bull.*, 2005, **53**, 27–31.
14 K. Hashizaki, H. Taguchi, C. Itoh, H. Sakai, M. Abe, Y. Saito and N. Ogawa, *Chem. Pharm. Bull.*, 2003, **51**, 815–820.
15 B. Mercadal, N. Beitel-White, K. N. Aycock, Q. Castellví, R. V. Davalos and A. Ivorra, *Ann. Biomed. Eng.*, 2020, **48**, 1451–1462.
16 C. R. Tracy, W. Kabbani and J. A. Cadeddu, *BJU Int.*, 2011, **107**, 1982–1987.
17 B. Rubinsky, G. Onik and P. Mikus, *Technol. Cancer Res. Treat.*, 2007, **6**, 37–48.
18 J. Lavee, G. Onik, P. Mikus and B. Rubinsky, *Heart Surg. Forum*, 2007, **10**, E162–E167.
19 A. Golberg and M. L. Yarmush, *IEEE Trans. Biomed. Eng.*, 2013, **60**, 707–714.
20 B. Geboers, H. J. Scheffer, P. M. Graybill, A. H. Ruarus, S. Nieuwenhuizen, R. S. Puijk, P. M. Van Den Tol, R. V. Davalos, B. Rubinsky, T. D. De Gruijl, D. Miklavčič and M. R. Meijerink, *Radiology*, 2020, **295**, 254–272.
21 L. Rems and D. Miklavcic, in *6th European Conference of the International Federation for Medical and Biological Engineering*, Springer Int. Publ. Switz, 2015.
22 J. T. Au, A. Mittra, T. J. Song, M. Cavnar, K. Jun, J. Carson, S. Gholami, D. Haddad, S. Gaujoux, S. Monette, P. Ezell, J. Wolchok and Y. Fong, *Surgery*, 2013, **154**, 496–503.
23 J. T. Au, J. Wong, A. Mittra, S. Carpenter, D. Haddad, J. Carson, S. Jayaraman, S. Monette, S. B. Solomon, P. Ezell and Y. Fong, *Surgery*, 2011, **150**, 474–479.
24 V. M. Ringel-Scaia, N. Beitel-White, M. F. Lorenzo, R. M. Brock, K. E. Huie, S. Coutermarsh-Ott, K. Eden, D. K. McDaniel, S. S. Verbridge, J. H. Rossmeisl, K. J. Oestreich, R. V. Davalos and I. C. Allen, *EBioMedicine*, 2019, **44**, 112–125.
25 B. Al-Sakere, F. André, C. Bernat, E. Connault, P. Opolon, R. V. Davalos, B. Rubinsky and L. M. Mir, *PLoS One*, 2007, **2**, e1135.
26 H. Cindrič, B. Kos and D. Miklavčič, *Slov. Med. J.*, 2021, **90**, 38–53.
27 M. Tarek, *Biophys. J.*, 2005, **88**, 4045–4053.
28 G. Kasparyan and J. S. Hub, *Phys. Rev. Lett.*, 2024, **132**, 148401.
29 L. Delemotte and M. Tarek, *J. Membr. Biol.*, 2012, **245**, 531–543.
30 M. L. Fernández, G. Marshall, F. Sagués and R. Reigada, *J. Phys. Chem. B*, 2010, **114**, 6855–6865.
31 M. Casciola, D. Bonhenry, M. Liberti, F. Apollonio and M. Tarek, *Bioelectrochemistry*, 2014, **100**, 11–17.
32 F. Guo, J. Wang, J. Zhou, K. Qian, H. Qu, P. Liu and S. Zhai, *RSC Adv.*, 2022, **12**, 24491–24500.
33 S. Mirshahi, B. Vahedi, S. O. Yazdani, M. Golab and A. Sazgarnia, *J. Mol. Model.*, 2024, **30**, 221.
34 M. K. Ahamed, M. A. S. Karal, M. Ahmed and S. Ahammed, *Eur. Biophys. J.*, 2020, **49**, 371–381.
35 R. Dimova and K. A. Riske, in *Handbook of Electroporation*, ed. D. Miklavcic, Springer International Publishing, Cham, 2016, pp. 1–18.
36 R. Dimova, N. Bezlyepkina, M. D. Jordö, R. L. Knorr, K. A. Riske, M. Staykova, P. M. Vlahovska, T. Yamamoto, P. Yang and R. Lipowsky, *Soft Matter*, 2009, **5**, 3201.
37 R. Dimova, K. A. Riske, S. Aranda, N. Bezlyepkina, R. L. Knorr and R. Lipowsky, *Soft Matter*, 2007, **3**, 817.
38 M. A. S. Karal, U. S. Orchi, M. Towhiduzzaman, M. K. Ahamed, M. Ahmed, S. Ahammed, N. A. Mokta, S. Sharmin and M. K. Sarkar, *Chem. Phys. Lipids*, 2020, **231**, 104935.
39 M. A. S. Karal, M. K. Ahamed, N. A. Mokta, M. Ahmed and S. Ahammed, *Eur. Biophys. J.*, 2020, **49**, 361–370.
40 M. K. Sarkar, M. A. S. Karal, M. Ahmed, M. K. Ahamed, S. Ahammed, S. Sharmin and S. U. A. Shibly, *PLoS One*, 2021, **16**, e0251690.
41 M. K. Sarkar, M. A. S. Karal, V. Levadny, M. Belaya, M. Ahmed, Md. K. Ahamed and S. Ahammed, *Eur. Biophys. J.*, 2022, **51**, 401–412.
42 M. A. Wadud, M. A. S. Karal, M. Moniruzzaman and M. M. O. Rashid, *PLoS One*, 2023, **18**, e0291496.
43 M. A. S. Karal, S. Sultana, M. M. Billah, M. Moniruzzaman, M. A. Wadud and R. C. Gosh, *PLoS One*, 2023, **18**, e0289087.
44 J. Derganc, Š. Zemljič-Jokhadar, B. Majaron and G. Kokot, *RSC Adv.*, 2023, **13**, 24830–24834.
45 Y. Sakuma, N. Kayamori, J. Tanaka, K. Haga, M. Imai and T. Kawakatsu, *Biophys. J.*, 2024, **123**, 489–501.
46 J. P. Reeves and R. M. Dowben, *J. Cell. Physiol.*, 1969, **73**, 49–60.
47 P. Walde, K. Cosentino, H. Engel and P. Stano, *ChemBioChem*, 2010, **11**, 848–865.
48 M. A. S. Karal, M. Rahman, M. K. Ahamed, S. U. A. Shibly, M. Ahmed and M. M. Shakil, *Eur. Biophys. J.*, 2019, **48**, 349–359.
49 R. Dimova, N. Bezlyepkina, M. D. Jordö, R. L. Knorr, K. A. Riske, M. Staykova, P. M. Vlahovska, T. Yamamoto, P. Yang and R. Lipowsky, *Soft Matter*, 2009, **5**, 3201.

© 2025 The Author(s). Published by the Royal Society of Chemistry

Open Access Article. Published on 11 November 2025. Downloaded on 1/20/2026 5:34:56 PM. This article is licensed under a Creative Commons Attribution-NonCommercial 3.0 Unported Licence.

50 K. A. Riske and R. Dimova, *Biophys. J.*, 2005, **88**, 1143–1155.
51 I. G. Abidor, V. B. Arakelyan, L. V. Chernomordik, Yu. A. Chizmadzhev, V. F. Pastushenko and M. P. Tarasevich, *J. Electroanal. Chem. Interfacial Electrochem.*, 1979, **104**, 37–52.
52 R. Dimova, K. A. Riske, S. Aranda, N. Bezlyepkina, R. L. Knorr and R. Lipowsky, *Soft Matter*, 2007, **3**, 817.
53 R. Lisin, B. Z. Ginzburg, M. Schlesinger and Y. Feldman, *Biochim. Biophys. Acta, Biomembr.*, 1996, **1280**, 34–40.
54 S. Tanizaki and M. Feig, *J. Chem. Phys.*, 2005, **122**, 124706.
55 W. Rawicz, K. C. Olbrich, T. McIntosh, D. Needham and E. Evans, *Biophys. J.*, 2000, **79**, 328–339.
56 S. A. Simon and T. J. McIntosh, in *Methods in Enzymology*, Academic Press, 1986, vol. 127, pp. 511–521.
57 M. K. Ahamed, M. A. S. Karal, M. Ahmed and S. Ahammed, *Eur. Biophys. J.*, 2020, **49**, 371–381.
58 M. Yamazaki, in *Advances in Planar Lipid Bilayers and Liposomes*, Academic Press, 2008, vol. 7, pp. 121–142.
59 M. A. S. Karal, M. K. Ahamed, M. Ahmed and Z. B. Mahbub, *RSC Adv.*, 2021, **11**, 29598–29619.
60 M. A. S. Karal, M. K. Ahamed, M. Rahman, M. Ahmed, M. M. Shakil and K. Siddique-e-Rabbani, *Eur. Biophys. J.*, 2019, **48**, 731–741.
61 S. Yuan, H. C. S. Chan and Z. Hu, *Wiley Interdiscip. Rev.: Comput. Mol. Sci.*, 2017, **7**, e1298.
62 S. Gorelov, A. Titov, O. Tolicheva, A. Konevega and A. Shvetsov, *J. Chem. Inf. Model.*, 2024, **64**, 6241–6246.
63 S. Jo, J. B. Lim, J. B. Klauda and W. Im, *Biophys. J.*, 2009, **97**, 50–58.
64 S. Jo, X. Cheng, J. Lee, S. Kim, S.-J. Park, D. S. Patel, A. H. Beaven, K. I. Lee, H. Rui, S. Park, H. S. Lee, B. Roux, A. D. MacKerell Jr, J. B. Klauda, Y. Qi and W. Im, *J. Comput. Chem.*, 2017, **38**, 1114–1124.
65 J. Lee, X. Cheng, J. M. Swails, M. S. Yeom, P. K. Eastman, J. A. Lemkul, S. Wei, J. Buckner, J. C. Jeong, Y. Qi, S. Jo, V. S. Pande, D. A. Case, C. L. I. Brooks, A. D. Jr. MacKerell, J. B. Klauda and W. Im, *J. Chem. Theory Comput.*, 2016, **12**, 405–413.
66 U. Essmann, L. Perera, M. L. Berkowitz, T. Darden, H. Lee and L. G. Pedersen, *J. Chem. Phys.*, 1995, **103**, 8577–8593.
67 G. Bussi, D. Donadio and M. Parrinello, *J. Chem. Phys.*, 2007, **126**, 014101.
68 M. Bernetti and G. Bussi, *J. Chem. Phys.*, 2020, **153**, 114107.
69 M. A. S. Karal, V. Levadnyy and M. Yamazaki, *Phys. Chem. Chem. Phys.*, 2016, **18**, 13487–13495.
70 V. Levadny, T. Tsuboi, M. Belaya and M. Yamazaki, *Langmuir*, 2013, **29**, 3848–3852.
71 M. A. S. Karal and M. Yamazaki, *J. Chem. Phys.*, 2015, **143**, 081103.
72 M. A. S. Karal, U. S. Orchi, M. Towhiduzzaman, M. K. Ahamed, M. Ahmed, S. Ahammed, N. A. Mokta, S. Sharmin and M. K. Sarkar, *Chem. Phys. Lipids*, 2020, **231**, 104935.
73 M. A. S. Karal, M. K. Ahamed, N. A. Mokta, M. Ahmed and S. Ahammed, *Eur. Biophys. J.*, 2020, **49**, 361–370.
74 E. Jaradat, A. Meziane and D. A. Lamprou, *Int. J. Pharm.*, 2024, **655**, 124077.
75 S. Melikishvili, A. Poturnayova, M. Ionov, M. Bryszewska, T. Vary, J. Cirak, M. Á. Muñoz-Fernández, R. Gomez-Ramirez, F. J. De La Mata and T. Hianik, *Biochim. Biophys. Acta, Biomembr.*, 2016, **1858**, 3005–3016.
76 O. Tirosh, Y. Barenholz, J. Katzhendler and A. Priev, *Biophys. J.*, 1998, **74**, 1371–1379.
77 A. S. Nosova, O. O. Koloskova, A. A. Nikonova, V. A. Simonova, V. V. Smirnov, D. Kudlay and M. R. Khaitov, *MedChemComm*, 2019, **10**, 369–377.
78 H. Hatakeyama, H. Akita and H. Harashima, *Biol. Pharm. Bull.*, 2013, **36**, 892–899.
79 M. Silvander, M. Johnsson and K. Edwards, *Chem. Phys. Lipids*, 1998, **97**, 15–26.
80 T. Kotnik, L. Rems, M. Tarek and D. Miklavčič, *Annu. Rev. Biophys.*, 2019, **48**, 63–91.
81 J. C. Weaver and Yu. A. Chizmadzhev, *Bioelectrochem. Bioenerg.*, 1996, **41**, 135–160.
82 R. Dimova, in *Advanced Electroporation Techniques in Biology and Medicine*, CRC Press, 2010.
83 Z. A. Levine and P. T. Vernier, *J. Membr. Biol.*, 2010, **236**, 27–36.
84 J.-M. Escoffre, D. S. Dean, M. Hubert, M.-P. Rols and C. Favard, *Eur. Biophys. J.*, 2007, **36**, 973–983.
85 M. J. Lopez and C. A. Hall, in *Physiology, Osmosis*, StatPearls Publishing, Treasure Island (FL), 2025.
86 T. B. Napotnik and D. Miklavčič, *Bioelectrochemistry*, 2018, **120**, 166–182.
87 C. Zhou and K. Liu, *Biomed. Eng. Online*, 2019, **18**, 123.
88 T. Kotnik, L. Rems, M. Tarek and D. Miklavčič, *Annu. Rev. Biophys.*, 2019, **48**, 63–91.
89 P. Marracino, L. Caramazza, M. Montagna, R. Ghahri, M. D'Abramo, M. Liberti and F. Apollonio, *Bioelectrochemistry*, 2022, **143**, 107987.
90 H. Leontiadou, A. E. Mark and S. J. Marrink, *Biophys. J.*, 2004, **86**, 2156–2164.
91 M. Kulma and G. Anderluh, *Cell. Mol. Life Sci.*, 2021, **78**, 6229–6249.
92 W. F. D. Bennett, N. Sapay and D. P. Tieleman, *Biophys. J.*, 2014, **106**, 210–219.
93 Y. Hu, S. K. Sinha and S. Patel, *Langmuir*, 2015, **31**, 6615–6631.
94 G. M. Cooper, in *The Cell: A Molecular Approach*, Sinauer Associates, 2nd edn, 2000.
95 B. Alberts, A. Johnson, J. Lewis, M. Raff, K. Roberts and P. Walter, in *Molecular Biology of the Cell*, Garland Science, 4th edn, 2002.
96 T. Portet and R. Dimova, *Biophys. J.*, 2010, **99**, 3264–3273.
97 R. Reigada, *Biochim. Biophys. Acta, Biomembr.*, 2014, **1838**, 814–821.
98 M. Ji, J. Xu, S. Yuan, Y. Liu, X. Xing, C. Jiang, L. Xue, C. Yang, F. Chu and Y. Jiang, *Comput. Theor. Chem.*, 2022, **1207**, 113487.
99 M. Tokman, J. H. Lee, Z. A. Levine, M.-C. Ho, M. E. Colvin and P. T. Vernier, *PLoS One*, 2013, **8**, e61111.
100 P. Ye, L. Huang and K. Zhao, *ACS Omega*, 2024, **9**, 50458–50465.

© 2025 The Author(s). Published by the Royal Society of Chemistry